Journal of Alloys and Compounds 707 (2017) 321–326

Contents lists available at ScienceDirect

Journal of Alloys and Compounds

journal homepage: http://www.elsevier.com/locate/jalcom

Size-dependent hardness and tensile plasticity of Ta-$Zr_{61}Cu_{17.5}Ni_{10}Al_{17.5}Si_4$ nanolaminates

C. Gu [a], F. Wang [b, **], P. Huang [a, *], K.W. Xu [a], T.J. Lu [b, c]

[a] State-Key Laboratory for Mechanical Behavior of Material, Xi'an Jiaotong University, Xi'an, 710049, China
[b] State Key Laboratory for Strength and Vibration of Mechanical Structures, Xi'an Jiaotong University, Xi'an, 710049, China
[c] MOE Key Laboratory for Multifunctional Materials and Structures, Xi'an Jiaotong University, Xi'an 710049, China

ARTICLE INFO

Article history:
Received 28 July 2016
Received in revised form
9 November 2016
Accepted 10 November 2016
Available online 13 November 2016

Keywords:
Amorphous
Crystalline
Nanolaminate
Plasticity
Size effect

ABSTRACT

Ta/$Zr_{61}Cu_{17.5}Ni_{10}Al_{17.5}Si_4$ crystalline/amorphous (C/A) nanolaminates with different Ta and ZrCuNiAlSi layer thicknesses were deposited by magnetron sputtering on both Si and polyimide substrates. Nanoindentation and uniaxial tensile tests were separately performed to study their size-dependent hardness and plasticity. Tensile plasticity was evaluated by considering both the tensile cracks and nanoindentation morphologies observed under scanning electron microscope (SEM). C/A nanolaminates with crystalline layer thickness of 40 nm and amorphous layer thickness of 5 nm exhibited the best tensile plasticity, which was much better than pure Ta and $Zr_{61}Cu_{17.5}Ni_{10}Al_{17.5}Si_4$ monolayers. For nanolaminates having identical Ta layer thickness, the hardness always increased with decreasing amorphous layer thickness. Combined with cross-sectional high resolution transmission electron microscopy (HRTEM) observation, the size-dependent deformation mechanisms of C/A nanolaminates were discussed.

1. Introduction

Although nanocrystalline and amorphous materials attracted tremendous attention due to their unique mechanical properties [1–4], the engineering application of these materials had been greatly limited by their poor plasticity. The poor plasticity mainly attributed to the increasingly difficulty for dislocation operation in nanocrystalline materials and the catastrophic failure through mature shear band (SB) formation and propagation in amorphous materials [5,6]. To solve this problem, combining nanocrystalline and amorphous nanoscale thin layers to form crystalline/amorphous (C/A) nanolaminates was proposed to effectively improve plasticity relative to either nanocrystalline or amorphous materials [7–9].

For a C/A nanolaminates, individual-layer-thickness dependent dislocation and shear transformation zone (STZ) motions inside the crystalline and amorphous thin layers, respectively, played crucial roles in determining its mechanical properties [7]. Other than size effects related to individual layer thickness, selection of lattice structure of the crystalline layers was also a crucial issue, which was not addressed until very recently. Previously, for nearly all the nanolaminates, face-center cubic (fcc) latticed Cu was chosen as the crystalline constituent layer [7,8,10–14], and only a few studies considered other lattice structures, *e.g.*, body-centered cubic (bcc) [9] and hexagonal close-packed (hcp) [15]. As crystalline layers having different lattice structures could exhibit quite different deformation behaviors because of their own unique slip systems, it is yet clear whether improved plasticity could be achieved by adding amorphous materials into bcc latticed metals and how the plastic deformation mechanism of nanolaminates is affected by amorphous layer thickness.

In the present study, bcc Ta and $Zr_{61}Cu_{17.5}Ni_{10}Al_{7.5}Si_4$ amorphous alloy were selected as the constituent materials to prepare Ta/$Zr_{61}Cu_{17.5}Ni_{10}Al_{7.5}Si_4$ C/A nanolaminates. By testing the mechanical properties of samples having different Ta and/or $Zr_{61}Cu_{17.5}Ni_{10}Al_{7.5}Si_4$ layer thicknesses, the optimized combination of individual layer thickness was investigated. The underlying deformation mechanisms were explored by examining the indentation morphologies, tensile cracks and atomic scale microstructures.

* Corresponding author.
** Corresponding author.
E-mail addresses: wangfei@mail.xjtu.edu.cn (F. Wang), huangping@mail.xjtu.edu.cn (P. Huang).

http://dx.doi.org/10.1016/j.jallcom.2016.11.156
0925-8388/

2. Experimental details

2.1. Material preparation

Ta/ZrCuNiAlSi nanolaminates with various individual layer thicknesses were deposited on both Si(100) and polyimide substrates via magnetron sputtering. For reference, monolayer Ta and ZrCuNiAlSi thin films were also prepared. Firstly, a circular polyimide substrate layer, diameter 50 mm, was placed on a pallet and then covered with a baffle with five rectangular holes (3 mm in width and 40 mm in length). Secondly, two fan-shaped silicon chips were fixed on the edge of a baffle. Finally, the deposition device was placed inside a vacuum chamber. Thin films of both C/A nanolaminates and monolayers were deposited on Si and polyimide substrates simultaneously in order to ensure the consistency of deposition parameters. Thin films deposited on Si substrates were used for nanoindentation testing, while those deposited on polyimide substrates were for tensile testing.

Before depositing, the direct-current (DC) power was connect with a 99.99% pure Ta target and the radio-frequency (RF) power was connect with a ZrCuNiAlSi alloy target. During depositing, the DC power and RF power were fixed at 100 W and 150 W, respectively. Ta and ZrCuNiAlSi monolayers were prepared by single operation of DC power and RF power, respectively, while the Ta/ZrCuNiAlSi nanolaminates were prepared by working alternatively with DC power and RF power. Two series of Ta/ZrCuNiAlSi nanolaminates were prepared. For seriesI, the thickness of Ta layer was fixed at 20 nm while ZrCuNiAlSi layer thickness was varied from 2.5 nm to 20 nm. For seriesII, the thickness of Ta layer was fixed at 40 nm and the ZrCuNiAlSi layer thickness was varied in the same manner as series I. For both series I and II thin films, the total film thickness was fixed as 1500 nm by carefully controlling the deposition time.

2.2. Mechanical behaviors

The hardness of all the samples was evaluated using a Nanoindenter XP system (MTS, Inc.) under Continuous Stiffness Measurement (CSM) mode, with a fixed strain rate of 0.05 s^{-1}. The indentation depth was fixed as 200 nm for hardness testing and the tip was Berkovich indenter with radius ~50 nm. For each measurement, 16 indents were carried out and at least 10 effective data were involved in the eventual analysis. In addition, deep indentations with penetration depth of 1500 nm were performed for each thin film sample to further characterize the deformation behavior. For each sample, tensile tests were also carried out via a Universal Testing Machine at a constant strain rate of 10^{-5} s^{-1}, and the gauge length and elongation were fixed as 30 mm and 10%, respectively.

2.3. Microstructural investigation

The microstructures of Ta/ZrCuNiAlSi nanolaminates, especially the Ta-ZrCuNiAlSi interface structures, were examined under HRTEM (JEOL JEM-2100 F operating at 200 KV). TEM sample was prepared by cutting a small piece from specimen deposited on Si substrate. Indentation morphologies and tensile cracks were observed under SEM.

3. Results and discussion

3.1. Deformation behaviors

The morphologies of tensile cracks were used to characterize the plasticity of all samples. Fig. 1 showed the SEM images of the tested samples, with low magnification (1 K) and high magnification (20 K) images separated by dashed lines in Fig. 1(a)–(j). For pure Ta and ZrCuNiAlSi thin films, cracks were clearly observed in both low and high magnification images as shown in Fig. 1(a) and (b). Similarly, cracks also appeared in all Ta(20)/Am(*x*) (*x* means a variable parameter with value of 2.5 nm, 5 nm, 10 nm or 20 nm) nanolaminates as shown in Fig. 1(c)–(f) (sample with Ta layer thickness of *m* nm and ZrCuNiAlSi layer thickness of *n* nm was referred as Ta(m)/Am(n) hereafter). In contrast to tensile testing of free standing films or bulk materials, where only a mature fracture formed, the formation of multiple cracks in the present study was attributed to the adhesion force between the deposited film and the polyimide substrate. Upon tensile deformation, the film was homogeneously elongated with polyimide. When the strain exceeded the breaking elongation of the film, cracks formed on its top surface and evenly distributed along the length direction. The cracks in the SEM image were caused by different elastic recovery percentages between the film and the polyimide. As the thickness of polyimide (200 μm) was much larger than the film (1.5 μm), the elastic recovery percentage of polyimide was negligibly affected by the film and should be, approximately, the same in all the samples. For a thin film deposited on polyimide, better plasticity means larger elongation with the polyimide, resulting in a narrow crack separation distance after elastic recovery. In extreme cases, if the plasticity of the film was better than the experimentally setting strain value, no crack would be observed.

The crack separation distance shown in Fig. 1 was an average of ten cracks which were distributed uniformly across the samples. As the values in Fig. 1(c)–(f) were larger than those in Fig. 1(a) and (b), the plasticity of Ta(20)/Am(x) nanolaminates was even worse than both monolayer Cu and ZrCuNiAlSi. In particular, upon increasing the Am layer thickness to 20 nm, the value shown in Fig. 1(f) was much larger than the other Ta(20)/Am(x) nanolaminates, corresponding to the worst plasticity among all the samples. By further increasing the thickness of Ta layer to 40 nm, the crack morphologies of Ta(40)/Am(x) became quite different: contrary to Ta(20)/Am(x) where the largest crack separation distance was observed in the sample having the thickest Am layer, the largest crack separation distance appeared in Ta(40)/Am(x) having the thinnest Am layer as shown in Fig. 1(g). Furthermore, Fig. 1(j) indicated that the crack separation distance of Ta(40)/Am(x) with the largest Am layer thickness, *i.e.*, Ta(40)/Am(20), was smaller than all other Ta(20)/Am(x), indicating an enhanced plasticity. For Ta(40)/Am(5) and Ta(40)/Am(10) shown in Fig. 1(h) and (i), respectively, cracks in both low and high magnification images were nearly invisible. Especially, note that the magnification of Ta(40)/Am(5) and Ta(40)/Am(10) in high magnification images was 25 K, larger than the others with 20 K magnification. These results indicated that plasticity had been effectively improved when the Ta layer thickness was set as 40 nm and Am layer thickness as 5 nm or 10 nm. As cracks in Ta(40)/Am(5) and Ta(40)/Am(10) were nearly the same, it was hard to clarify which sample had the better plasticity. Consequently, residue nanoindentation morphologies of these samples were investigated as shown in Fig. 2.

Fig. 2(a) and (f) presented the indentation morphologies of monolayer Ta and ZrCuNiAlSi, respectively. Cracks and shear bands (SBs) in Fig. 2(a) and (f) represented typical indentation morphologies of brittleness crystalline and amorphous phase materials. However, the indentation morphologies became more complex when Am layers were added into crystalline Ta. For Ta(20)/Am(x), a switch from cracks to SBs was observed when Am layer thickness was increased from 2.5 nm to 20 nm as shown in Fig. 2(b)–(e). Interestingly, for Ta(20)/Am(5), cracks and SBs were both observed. In contrast, for Ta(40)/Am(x), no SBs was observed as Ta layer thickness was increased. For Ta(40)/Am(10), in particular, both SBs

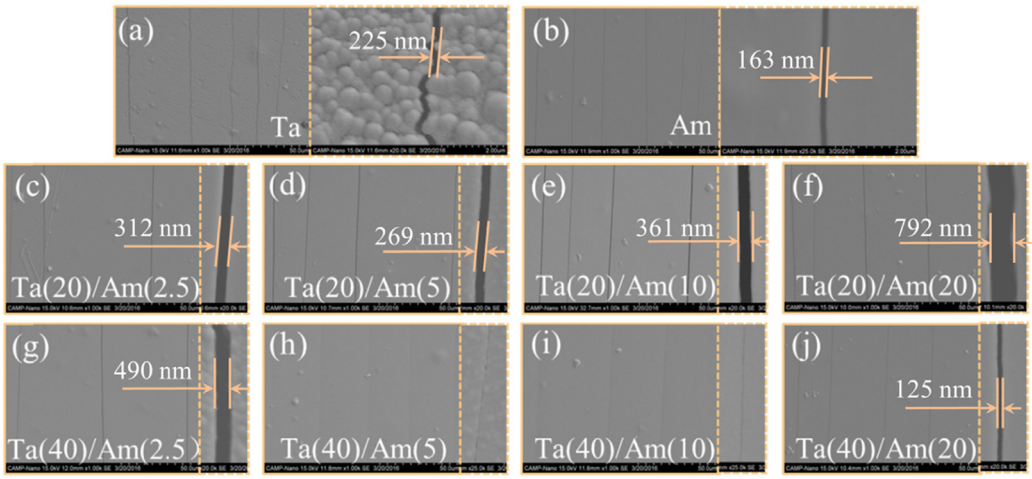

Fig. 1. SEM images of samples after tensile test: (a) monolayer Ta, (b) monolayer ZrCuNiAlSi, (c) Ta(20)/Am(2.5), (d) Ta(20)/Am(5), (e) Ta(20)/Am(10), (f) Ta(20)/Am(20), (g) Ta(40)/Am(2.5), (h) Ta(40)/Am(5), (i) Ta(40)/Am(10) and (j) Ta(40)/Am(20).

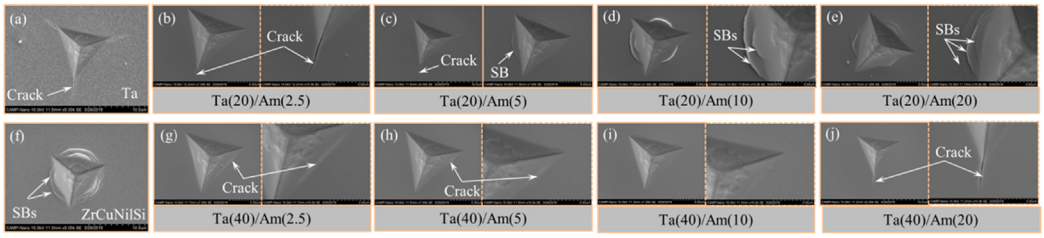

Fig. 2. Nanoindentation morphologies of (a) monolayer Ta, (b) Ta(20)/Am(2.5), (c) Ta(20)/Am(5), (d) Ta(20)/Am(10), (e) Ta(20)/Am(20), (f) monolayer ZrCuNiAlSi, (g) Ta(40)/Am(2.5), (h) Ta(40)/Am(5), (i) Ta(40)/Am(10) and (j) Ta(40)/Am(20).

and cracks were inhibited due likely to its significantly enhanced plasticity.

3.2. Microstructures

For a C/A nanolaminate system, the structure of NC layer, Am layer and interface played important roles in its deformation behavior. As a result, cross-sectional microstructure near the interface was examined with TEM. Fig. 3 showed the TEM images of samples with different Ta layer and Am layer thicknesses. Fig. 3(a)–(c) displayed the bright field, dark field and HRTEM images of Ta(20)/Am(10), respectively. In Fig. 3(a) and (b), both Ta layer and Am layer could be clearly distinguished, as marked by arrows. The HRTEM image of Fig. 3(c) indicated that the Ta-Am interface was very straight, with no crystallization in Am layer. As Ta layer thickness was increased, the bright field, dark field and HRTEM images of Ta(40)/Am(10) were shown in Fig. 3(d)–(f). Both Ta layer and Am layer could be clearly distinguished in Fig. 3(d) and (e), and the straight interface structure shown in Fig. 3(f) was similar to Ta(20)/Am(10). The microstructure of Ta(40)/Am(2.5), which had the thinnest Am layer, was shown in Fig. 3(g)–(i).

The results of Fig. 3 suggested that the modulation structure of C/A nanolaminates was clear and the Ta layer did not grow through the Am layer even if the thickness of Am layer was only a few nanometers.

3.3. Nanoindentation hardness and deformation mechanisms

Fig. 4 plotted the nanoindentation hardness of Ta/ZrCuNiAlSi nanolaminates as a function of Am layer thickness, which exhibited a good linear relationship for both Ta(40)/Am(x) and Ta(20)/Am(x). For reference, the hardness data for monolayer Ta and ZrCuNiAlSi were also presented in Fig. 4 as indicated by dotted lines. Within the relatively small range of Am layer thickness, the hardness of Ta/Am nanolaminates was enhanced relative to pure Ta. For the present two series of samples, as the thickness of Ta layer was fixed, the size effect of Am layer was proposed as the dominant strengthening mechanism.

For Am layer, the size-dependent critical stress required for SB formation was given as [14,16]:

$$\sigma = \sqrt{2^{3/2}\Gamma E/h} \tag{1}$$

where E was the Young modulus, Γ was the energy per unit area of SB, and h was the Am layer thickness. Equation (1) indicated that the strength of Am layer would be enhanced when its thickness was decreased, which was consistent with the present hardness results. However, numerous existing studies had proved that the strength of amorphous thin films or pillars was independent of sample size in the large thickness or diameter range [16–19]. As a result, equation (1) should hold below a critical Am layer thickness, for the hardness of Am layer should be constant for larger thicknesses. It had been demonstrated that the transition from size-independent to size-dependent hardness was mainly attributed to deformation mechanism transformation in amorphous materials [20–23]. For instance, the strength of PdSi amorphous pillars was found to be independent of pillar diameters in the large diameter range [16]. Upon decreasing the diameter of PdSi amorphous pillars to ~140 nm, the deformation mode changed from SB propagation to homogeneous flow, causing decreased strength. In what follows,

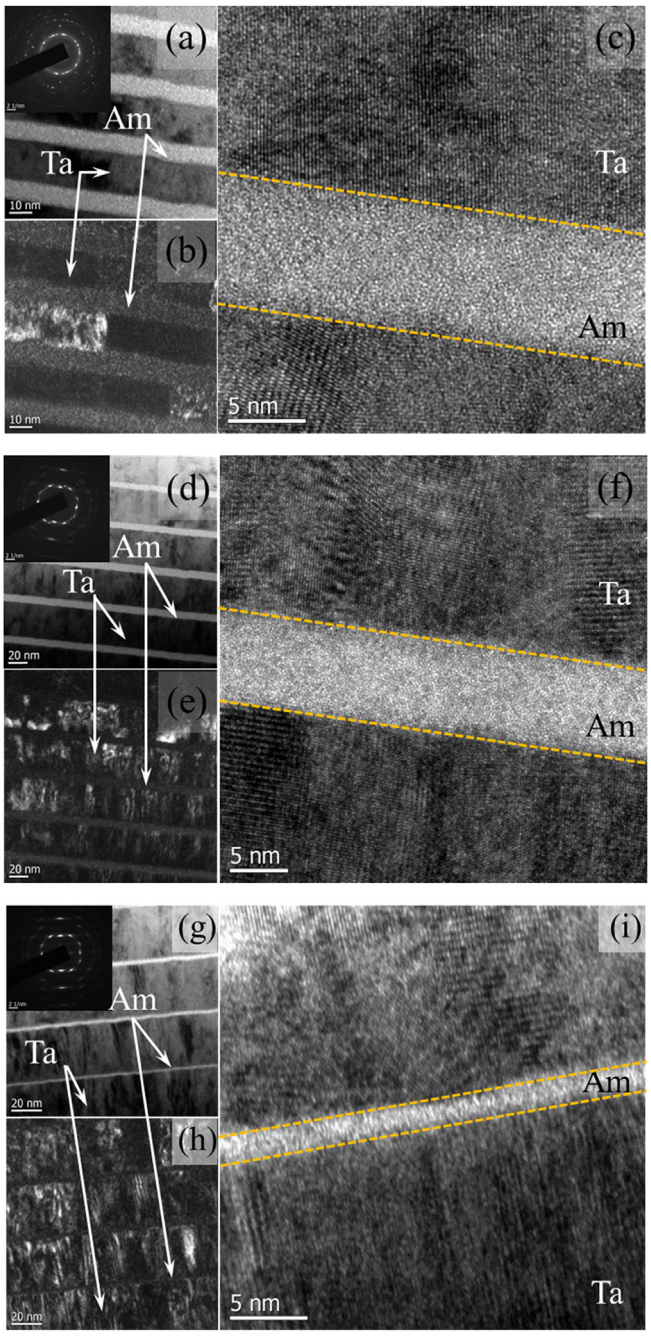

Fig. 3. Cross-sectional TEM images of Ta/Am nanolaminates: (a) bright field images of Ta(20)/Am(10), (b) dark field images of Ta(20)/Am(10), (c) HRTEM images of Ta(20)/Am(10),(d) bright field images of Ta(40)/Am(10), (d) dark field images of Ta(40)/Am(10), (e) HRTEM images of Ta(40)/Am(10), (f) bright field images of Ta(40)/Am(2.5), (g) dark field images of Ta(40)/Am(2.5), and (h) HRTEM images of Ta(40)/Am(2.5).

the condition under which equation (1) holds was confirmed and the deformation behavior of Am layer in a nanolaminate system was discussed.

Wang et al. [7] indicated that there existed a critical size L_{inc}, below which STZs could hardly develop into mature SBs, and pointed out that this critical size was close to the thickness of SBs. Zhang et al. [24] estimated the thickness of SBs in different metallic glasses. In particular, for a pentabasic $Zr_{57}Ti_5Cu_{20}Ni_8Al_{10}$ metallic glass, which had quite similar alloy components to the present study, the thickness of SB was about 20 nm. Consequently, in the

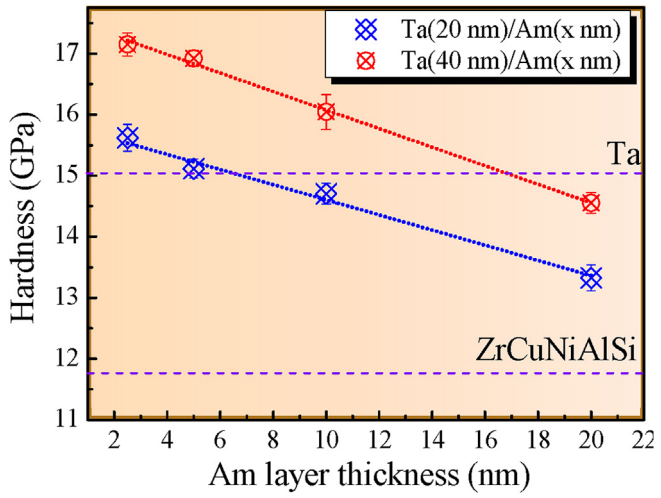

Fig. 4. Nanoindentation hardness of monolayer Ta and ZrCuNiAlSi as well as Ta/Am nanolaminates.

present study, it was expected that different mechanical responses would occur when the Am layer thickness was higher or lower than 20 nm. When the Am layer thickness was higher than 20 nm, SBs would easily nucleate and propagate under the applied stress. Correspondingly, the hardness of Am layer was size independent, equal to that of monolayer Am. In sharp contrast, when the Am layer thickness was dropped below 20 nm, the lack of geometric condition for SBs nucleation would cause significant size effect on hardness.

In equation (1), parameters Γ and E were only alloy components dependent and hence both would not vary when Am layer thickness was changed. As a result, the size dependent hardness H_s should be proportional to $h^{-1/2}$ according to equation (1). In order to calculate the slope of H_s curve, at least two hardness values in the curve should be confirmed. The first value confirmed would be that when the Am layer had a thickness of 20 nm, at which its hardness was equal to that of monolayer ZrCuNiAlSi as previously mentioned. The second value could be confirmed by examining the indentation morphology of Fig. 2(c). The indentation morphology of Ta(20)/Am(5) shown in Fig. 2(c) contained both cracks and SBs, which indicated that the deformation mechanism was randomly dominated by either crystalline Ta layer or Am layer. In this case, only if the hardness of Ta layer was the same as Am layer, the nanoindentation hardness of the whole nanolaminate could be the same even if indentation morphologies in different tests were different. Then the second value was confirmed, *i.e.*, when the thickness of Am layer was 5 nm and the hardness was equal to monolayer Ta: the corresponding hardness curve of H_s was plotted in Fig. 5. The hardness value was further calculated using the role of mixture (ROM), as:

$$H_{ROM} = H_{Ta} \cdot f_{Ta} + H_{Am} \cdot f_{Am} \quad (2)$$

where H_{Ta} and H_{am} were the hardness of Ta layer and Am layer, and f_{Ta} and f_{Am} were the volume fraction of Ta and Am layer, respectively. By calculating hardness from equation (2) and converting f_{Ta} and f_{Am} into the $h^{-1/2}$ coordinate, the H_{ROM} versus $h^{-1/2}$ curve was shown in Fig. 5. The result indicated that the hardness calculated by ROM fitted well with the experimental values of Ta(20)/Am(x) nanolaminates. Consequently, the strengthening mechanism of Ta(20)/Am(x) was dominated by both Ta and Am layers rather than dominated by a single layer as suggested by previous studies [13,14]. However, that the ROM results agreed well with

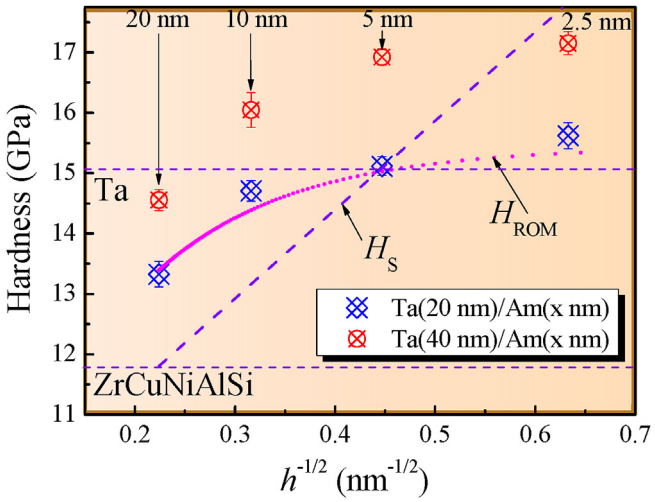

Fig. 5. Nanoindentation hardness vs. $h^{-1/2}$ curves of Ta/Am nanolaminates.

experimental data also indicated that the Ta-Am interface had little effect on the deformation mechanism of Ta(20)/Am(x). While the amorphous-crystalline interface (ACI) played an important role in coordinating the plastic deformation, the plasticity of Ta(20)/Am(x) was hardly improved. This was consistent with the results shown in Fig. 1(c)–(f), in which cracks were clearly observed.

In contrast, the hardness of Ta(40)/Am(x) was much higher than both Ta and H_{ROM} when Am layer thickness became smaller than 10 nm. As a result, an alternative deformation mechanism different from that of Ta(20)/Am(x) should be activated. For Ta(40)/Am(x), SBs were inhibited as shown in Fig. 2(g)–(j) which was quite different from Ta(20)/Am(x). The inhibition of SBs by a thicker crystalline layer was consistent with a previous study [15]. MD simulation results [7] indicated that in C/A nanolaminates, ACI could be dislocation emission and absorption sources except for grain boundaries in crystalline layers. The inhibition effect was mainly attributed to the motion of dislocations triggered by the nucleated SBs. The kinetic energy of SBs would be released by dislocation motion, and then the activated SBs were prohibited by ACIs due to the lack of energy condition for further propagation. Consequently, the absence of SBs in Fig. 2(g)–(j) was likely caused by the enhanced ACI effect in Ta(40)/Am(x). Although ACIs played an important role in the deformation behavior of Ta(40)/Am(x), only the plasticity of Ta(40)/Am(10) was significantly improved as shown in Figs. 1(i) and 2(i). Generally, the absorption of dislocations in ACIs was always accompanied with triggered STZs near ACIs. The triggered STZs would move to the deep Am layer or assist with ACI sliding to accommodate the plastic deformation. For Ta(40)/Am(20), the movement of STZs was confined in a finite area near ACIs which could be named as soft area. The area in the middle of the Am layer was named as hard area. While the mobility of soft area was better than hard area, where no STZs were triggered, stress concentration would occur in the area between soft area and hard area during plastic deformation. Cracks would nucleate in this area when the applied stress exceeded the slip resistance of Ta layer. This process could be confirmed by the fact that the hardness of Ta(40)/Am(20) was quite close to that of monolayer Ta. While the Am layer thickness was reduced to 10 nm, the thickness of hard area also decreased. As a result, soft area could accommodate most of the plastic deformation and the plasticity was greatly enhanced. Further, when STZs moved deep into the Am layer, the resistance from ACI on the opposite side would enhance the hardness. As the Am layer thickness was further reduced, the trigger of STZs became harder due to increased resistance from ACI on the opposite side or even because the geometric condition for the motion of STZs was lost. Therefore, while the hardness of Ta(40)/Am(5) and Ta(40)/Am(2.5) was both further increased, their plasticity was decreased as a result of the lack of STZs to accommodate the plastic deformation process.

4. Conclusion

Two series of Ta/ZrCuNiAlSi nanolaminates were prepared by adding thin ZrCuNiAlSi amorphous layers into Ta matrix. For seriesI, *i.e.*, Ta(20 nm)/Am(x nm) (x = 2.5, 5, 10 or 20) nanolaminates, the thickness of Ta layer was fixed at 20 nm and the Am layer thickness was varied from 2.5 nm to 20 nm; for seriesII, *i.e.*, Ta(40 nm)/Am(x nm) (x = 2.5, 5, 10 or 20) nanolaminates, the thickness of Ta layer was fixed at 40 nm and the Am layer thickness was varied in the same manner as seriesI. The results indicated that when the Ta layer is 20 nm, the hardness of Ta(20 nm)/Am(x nm) increases with decreasing Am layer thickness, which is consistent with that calculated by the role of mixture. It is demonstrated that amorphous-crystalline interfaces have little effect on the deformation behavior of these nanolaminates. As a result, the plasticity of Ta(20 nm)/Am(x nm) can hardly be improved due to lack of triggered shear transformation zones near amorphous-crystalline interfaces. On the contrary, amorphous-crystalline interfaces play an important role in Ta(40 nm)/Am(x nm). Due to the motion of dislocations and the trigger of shear transformation zones near amorphous-crystalline interfaces, the plastic strain can be coordinated by the deformation of amorphous layer and the plasticity is improved. Specifically, the plastic strain of Ta(40 nm)/Am(10 nm) is greatly enhanced (close to 10%), and is much higher than that of monolayer Ta and ZrCuNiAlSi thin films. While reducing the amorphous layer thickness to less than 10 nm, the trigger of shear transformation zones is affected by amorphous-crystalline interface on the opposite side and becomes difficult, which cause a lower plasticity but a further increased hardness.

Acknowledgements

The present work was supported by the National Natural Science Foundation of China (51171141, 51271141, and 51471131).

References

[1] M.A. Meyers, A. Mishra, D.J. Benson, Prog. Mater. Sci. 51 (2006) 427–556.
[2] K.S. Kumar, H. Van Swygenhoven, S. Suresh, Acta Mater. 51 (2003) 5743–5774.
[3] M.M. Trexler, N.N. Thadhani, Prog. Mater. Sci. 55 (2010) 759–839.
[4] U. Ramamurty, S. Jana, Y. Kawamura, K. Chattopadhyay, Acta Mater. 53 (2005) 705–717.
[5] M. Dao, L. Lu, R. Asaro, J. Dehosson, E. Ma, Acta Mater. 55 (2007) 4041–4065.
[6] Y. Huang, J.C. Khong, T. Connolley, J. Mi, Int. J. Plast. 60 (2014) 87–100.
[7] Y. Wang, J. Li, A.V. Hamza, T.W. Barbee Jr., Proc. Natl. Acad. Sci. U. S. A. 104 (2007) 11155–11160.
[8] J.Y. Kim, D. Jang, J.R. Greer, Adv. Funct. Mater. 21 (2011) 4550–4554.
[9] H.S. Chou, X.H. Du, C.J. Lee, J.C. Huang, Intermetallics 19 (2011) 1047–1051.
[10] I. Knorr, N.M. Cordero, E.T. Lilleodden, C.A. Volkert, Acta Mater. 61 (2013) 4984–4995.
[11] A. Donohue, F. Spaepen, R.G. Hoagland, A. Misra, Appl. Phys. Lett. 91 (2007) 241905.
[12] H.S. Huang, H.J. Pei, Y.C. Chang, C.J. Lee, J.C. Huang, Thin Solid Films 529 (2013) 177–180.
[13] W. Guo, E. Jägle, J. Yao, V. Maier, S. Korte-Kerzel, J.M. Schneider, D. Raabe, Acta Mater. 80 (2014) 94–106.
[14] J.Y. Zhang, G. Liu, S.Y. Lei, J.J. Niu, J. Sun, Acta Mater. 60 (2012) 7183–7196.
[15] M.C. Liu, C.J. Lee, Y.H. Lai, J.C. Huang, Thin Solid Films 518 (2010) 7295–7299.
[16] C.A. Volkert, A. Donohue, F. Spaepen, J. Appl. Phys. 103 (2008) 083539.
[17] X. Wang, F. Jiang, H. Hahn, J. Li, H. Gleiter, J. Sun, J. Fang, Scr. Mater. 116 (2016) 95–99.
[18] C.Q. Chen, Y.T. Pei, J.T.M. De Hosson, Acta Mater. 58 (2010) 189–200.
[19] M. Ghidelli, S. Gravier, J.J. Blandin, P. Djemia, F. Mompiou, G. Abadias,

J.P. Raskin, T. Pardoen, Acta Mater. 90 (2015) 232–241.
[20] M. Ghidelli, S. Gravier, J.-J. Blandin, J.-P. Raskin, F. Lani, T. Pardoen, Scr. Mater. 89 (2014) 9–12.
[21] F.F. Wu, S.S. Jiang, R.D. Zhao, Q. Zhou, G.A. Zhang, X.F. Wu, Mater. Sci. Eng. A 646 (2015) 272–278.
[22] C.C. Wang, J. Ding, Y.Q. Cheng, J.C. Wan, L. Tian, J. Sun, Z.W. Shan, J. Li, E. Ma, Acta Mater. 60 (2012) 5370–5379.
[23] C. Zhong, H. Zhang, Q.P. Cao, X.D. Wang, D.X. Zhang, J.Z. Jiang, Scr. Mater. 101 (2015) 48–51.
[24] Y. Zhang, A.L. Greer, Appl. Phys. Lett. 89 (2006) 071907.